One-pot synthesis of platinum₃cobalt nanoflowers with enhanced oxygen reduction and methanol oxidation
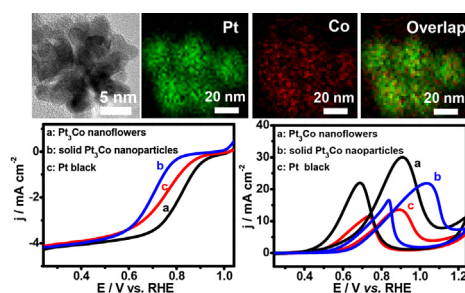
Jie-Ning Zheng, Li-Li He, Chen Chen, Ai-Jun Wang[*], Ke-Fu Ma, Jiu-Ju Feng[*]

College of Geography and Environmental Science, College of Chemistry and Life Science, Zhejiang Normal University, Jinhua 321004, China

HIGHLIGHTS

- Pt₃Co nanoflowers are prepared by a simple solvolthermal method.
- Pt₃Co nanoflowers display the enhanced electrocatalytic activity for ORR dominated by a four-electron pathway.
- Pt₃Co nanoflowers show the improved electrocatalytic property and high stability towards MOR.

GRAPHICAL ABSTRACT

ARTICLE INFO

ABSTRACT

Herein, a simple one-pot approach is developed for preparation of Pt₃Co nanoflowers by co-reduction of Pt (II) acetylacetonate (Pt(acac)₂) and Co (III) acetylacetonate (Co(acac)₃) in oleylamine, without any seed or template. It is found that hexadecylpyridinium chloride monohydrate (HDPC) is served as both the stabilizing and structuring-directing agent that plays an important role in the formation of well-dispersed flower-like Pt₃Co nanoparticles. The as-prepared Pt₃Co nanoflowers show the enhanced catalytic performance for oxygen reduction reaction (ORR) in comparison with solid Pt₃Co nanoparticles and commercial Pt black catalysts, dominated by a four-electron pathway based on the Koutecky–Levich equation. Meanwhile, Pt₃Co nanoflowers exhibit the improved catalytic activity and long-term stability towards methanol oxidation reaction (MOR), using solid Pt₃Co nanoparticles and commercial Pt black catalysts as references. The improved catalytic features of Pt₃Co nanoflowers are mainly attributed to the porous three-dimensionally interconnected structures, enlarged specific surface area, ligand effect and bifunctional mechanism between Pt and Co. The as-developed method provides a promising pathway for preparation of highly efficient electrocatalysts for ORR and MOR.

© 2014 Elsevier B.V. All rights reserved.

1. Introduction

Recently, direct methanol fuel cells (DMFCs) have attracted increasing attention for the advantages of high power density, ease of handling, and low operating temperature [1,2]. There are two major reactions involved: oxygen reduction reaction

(ORR) on the cathode and methanol oxidation reaction (MOR) on the anode. In these systems, Pt and Pt-based catalysts are widely used as efficient anode and cathode catalysts in acid media [3,4].

However, the durability of Pt-based catalysts can be compromised, owing to Ostwald ripening during the electrocatalytic process [5]. Besides, the generated CO-like intermediates have tendency to occupy the active sites of the catalyst surfaces, leading to the "poisoning" phenomenon on the catalysts, which is a major problem to the maintenance of their high catalytic activity [6].

* Corresponding authors.
E-mail addresses: ajwang@zjnu.cn, ajwangnju@gmail.com (A.-J. Wang), jjfeng@zjnu.cn (J.-J. Feng).

Moreover, high cost and scare resource of Pt severely limit their commercial applications in DMFCs [7].

To date, alloying Pt with relatively cheap metals (e.g., Pd, Au, Ag, Cu, and Ru) [8–12] demonstrates the best route to improve the catalytic activity and reduce the use of Pt. Impressively, introducing non-precious 3d transition metals (i.e. Fe, Co, Ni, and Sn) is proved to be the most available method for the enhanced catalytic performance of Pt [13–16]. This is ascribed to the special bifunctional mechanism of the alloyed bimetals and the regarding electronic effects [17–19], as further confirmed by PtCo alloyed networks with higher activity and better stability for MOR in comparison with Pt nanoparticles [20]. Based on the density functional theory, PtNi alloys were manifested the enhanced catalytic activity towards ORR [21], owing to the modified electronic structure of Pt by Ni.

Among the Pt-based catalysts, PtCo alloys are fascinating for their improved catalytic performance towards ORR and MOR [22–25]. Kwon and co-workers synthesized Pt_3Co nanoparticles (2–3 nm) with Pt-enriched shells on a carbon support, which showed the improved catalytic performance towards ORR in comparison with commercial Pt/C catalyst [26]. Fang et al. fabricated (100)-facet-terminated Pt_3Co nanocubes with the enhanced catalytic activity for MOR in comparison with Pt nanocubes [27]. Qiu's group prepared nanoporous PtCo alloys with the improved catalytic activity towards MOR [23].

However, synthesis of PtCo alloyed nanoparticles is quite a challenging task because of the large difference in standard reduction potential between these two metal ions and the distinct atom sizes [20,28]. Thus, great efforts have been devoted to the synthesis of PtCo nanoparticles. For example, Fang and co-workers synthesized Pt_3Co nanocubes with the help of oleylamine, oleic acid, and $W(CO)_6$ by varying the temperature from 130 to 240 °C [27]. Schaak et al. developed a two-step process for synthesis of hollow PtCo nanospheres, with the assistance of a sacrificial template [29]. Yang's group constructed PtCo nanorods in ionic liquid at 350 °C, using cetyltrimethylammonium bromide (CTAB) as a capping reagent [30]. Nevertheless, the high reaction temperature and complex operation steps limit their large-scale preparation.

As the catalytic reaction usually occurs on the catalyst surface, it is necessary and practical to fabricate a catalyst with enlarged surface area, lower noble metal loading, and improved catalytic activity. Porous three-dimensional nanocrystals are the ideal candidates to provide large surface areas and supply abundant active sites for reactant molecules [31], and thereby attract tremendous interest. Besides, their particular interconnected structures can effectively suppress the Ostwalding ripening effects, leading to the improved stability of the catalyst [32,33]. Up to now, great progress has been made for synthesis of bimetallic porous nanostructures, including porous Pd nanoparticles [34,35], PtPd nanoflowers [31], porous Pt_3Ni nanocrystals [36], and AuPd nanoflowers [37]. However, few studies are involved in the preparation of PtCo nanoflowers.

In this report, a one-pot synthesis strategy was developed for fabrication of Pt_3Co nanoflowers by co-reduction of Pt (II) acetylacetonate ($Pt(acac)_2$) and Co (III) acetylacetonate ($Co(acac)_3$) using oleylamine as a reducing agent and solvent, and HDPC as a stabilizing and structuring-directing agent. The electrocatalytic activity and stability of Pt_3Co nanoflowers were examined, using ORR and MOR as model systems.

2. Experimental section

2.1. Chemicals

$Pt(acac)_2$, $Co(acac)_3$, oleylamine, HDPC, and commercial Pt black were supplied from Aladdin Chemical Reagent Company (Shanghai,

China). Other chemicals were of analytical grade and used without further purification. All aqueous solutions were prepared with twice-distilled water throughout the whole experiments.

2.2. Synthesis of Pt_3Co nanoflowers

For typical synthesis of Pt_3Co nanoflowers, 100 mg of HDPC was dissolved into 20 mL of oleylamine under gentle agitation, and ultrasonicated for 30 min to obtain a homogenous solution. Then, 0.020 g of $Pt(acac)_2$ and 0.018 g of $Co(acac)_3$ were put into the mixed solution under stirring. After ultrasonication for another 30 min, the mixture was transferred into a Teflon-lined stainless autoclave. The autoclave was maintained at 170 °C for 24 h, and allowed to cool to room temperature naturally. The black precipitate was collected and thoroughly washed with ethanol, followed by dispersing in cyclohexane. Solid Pt_3Co nanoparticles were prepared in the absence of HDPC, while other conditions were kept constant.

2.3. Characterization

The detailed morphology, crystal structure, and composition of the samples were determined by transmission electron microscopy (TEM), high resolution TEM (HRTEM), high-angle annular dark-field scanning transmission electron microscopy (HAADF-STEM), and energy-dispersive X-ray spectroscopy (EDS) on a JEM-2100F microscope operated at an acceleration voltage of 200 kV. X-ray photoelectron spectroscopy (XPS) measurements were performed with a Thermo VG ESCALAB 250 spectrometer with an Al Kα X-ray radiation (1486.6 eV photons) for excitation operated at 120 W. X-ray diffraction (XRD) spectra were acquired on a Philips PW3040/60 diffractometer using Cu Kα radiation source ($\lambda = 0.15405$ nm).

2.4. Electrochemical measurements

The electrochemical measurements were carried out on a CHI832b electrochemical workstation (CH Instruments, Chenhua Co., Shanghai, China). A conventional three-electrode system was used for all the electrochemical experiments, which consists of a Pt wire as counter electrode, a saturated calomel reference electrode (SCE) as reference electrode, and a bare or modified glassy carbon electrode (GCE, 3 mm in diameter) or rotating disk electrode (RDE, 4 mm in diameter) as working electrode. Besides, the RDE experiments were carried out on a PAR model 616 RDE. All the potentials here were reported with respect to the reversible hydrogen electrode (RHE), if not stated otherwise.

For construction of the catalysts modified electrodes, 6 and 10 μL of the aqueous suspensions (1.0 mg mL^{-1}) were dropped onto the clean GCE and RDE surfaces with a microsyringe and dried in air, respectively, followed by casting 3 and 5 μL of Nafion (0.05 wt%) to tightly combine the catalyst on the electrode surfaces.

As known, CO is usually regarded as a major poison intermediate for Pt catalysts in alcohol oxidation process. Thus, CO stripping serves as a model probe to evaluate CO tolerance of a catalyst. CO-stripping measurements were performed as follows: CO was bubbled for 15 min to form CO adlayer on the surface of the catalyst at 0.1 V. Excess CO in the solution was purged with N_2 for 20 min and CO-stripping voltammograms were recorded via oxidizing the pre-adsorbed CO in 0.1 M $HClO_4$ at a scan rate of 50 mV s^{-1}. Cyclic voltammograms (CVs) were acquired with or without 1.0 M methanol in a potential window from -0.2 to 1.0 V ($vs.$ SCE) in 0.1 M $HClO_4$ at a scan rate of 50 mV s^{-1}. The amperometric current−time ($i−t$) curves were obtained at a fixed potential of 0.85 V for 6000 s in 1.0 M methanol + 0.1 M $HClO_4$. The electrochemically active surface area (ECSA) of a catalyst was calculated from the integrated
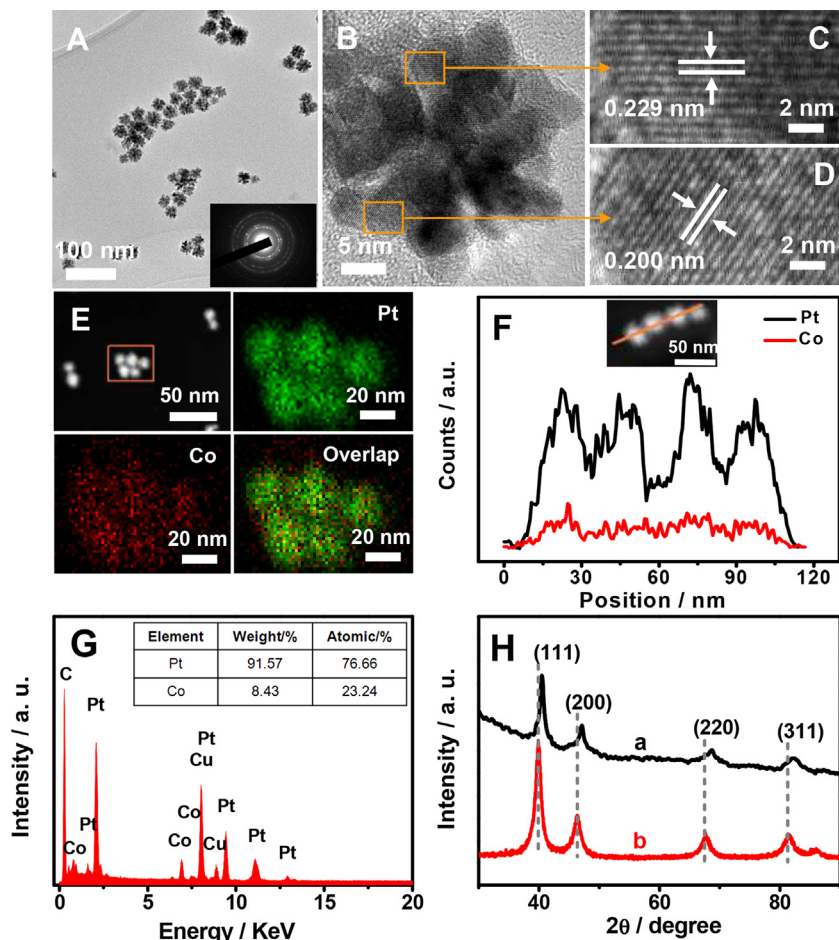
Fig. 1. (A) TEM and (B–D) HRTEM, and (E) HAADF-STEM–EDS mapping images of Pt$_3$Co nanoflowers. (F) The HAADF-STEM image and cross-sectional compositional line profile of a Pt$_3$Co nanoflower. (G) EDS pattern of Pt$_3$Co nanoflowers. (H) XRD patterns of Pt$_3$Co nanoflowers (curve a) and Pt black (curve b). Inset shows the corresponding SAED pattern.

hydrogen desorption region after double-layer correction, using 0.21 C cm^{-2} as the conversion factor [38].

The ORR polarization curves were recorded in O$_2$-saturated 0.1 M HClO$_4$ with a sweep rate of 5 mV s^{-1} at various rotation speeds ranging from 100 to 2500 rpm. The Koutecky–Levich plots (obtained by using the inverse current density (j^{-1}) as a function of the inverse of the square root of the rotation rate ($\omega^{-1/2}$)) were analyzed at 0.4 V. The slopes of the linear fitting lines were used to calculate the number of transferred electrons (n) according to the Koutecky–Levich equation [3,9]:

$$\frac{1}{i} = \frac{1}{i_k} + \frac{1}{i_d} = \frac{1}{i_k} + \frac{1}{B\omega^{1/2}} \tag{1}$$

$$B = 0.2nFC_0D_0^{2/3}\nu^{-1/6} \tag{2}$$

where i is the measured current, i_k is the kinetic current, i_d is the diffusion-limiting current, ω is the speed, n is the number of the transferred electrons, F is the Faraday constant (96485 C mol^{-1}), C_0 is the oxygen solubility (1.26×10^{-3} mol L^{-1}), D_0 is the oxygen diffusivity (1.93×10^{-5} cm^2 s^{-1}), and ν is the kinetic viscosity of the electrolyte (0.01 cm^2 s^{-1}) [39]. By putting these parameters into the Equation (2), $B = 0.0376n$. And B factor can be calculated from the inverse of the as-mentioned slopes.

The accelerated durability test (ADT) was carried out in 0.1 M HClO$_4$ by applying linear potential sweeps between −0.2 and 1.0 V (*vs.* SCE) for 1000 cycles at 50 mV s^{-1}.

3. Results and discussion

As can be seen from low-resolution TEM image (Fig. 1A), the as-prepared product contains a lot of well-defined flower-like nano-structures, with an averaged size of 24 nm. Furthermore, HRTEM image displays an individual flower with porous three-dimensional nanostructure, which is composed of many tiny particles with the averaged size of 5 nm (Fig. 1B).

The selected-area electron diffraction (SAED, inset in Fig. 1A) pattern demonstrates polycrystalline nature of Pt$_3$Co nanoflowers. Besides, Fig. 1C and D show the interplanar spacings determined from different tiny particles with the values of 0.229 and 0.200 nm, corresponding to the (111) and (200) planes of the face-centered cubic (fcc) Pt$_3$Co alloys, respectively [40,41]. These results indicate the formation of Pt$_3$Co alloyed phase.

HAADF-STEM elemental mapping images (Fig. 1E) and the corresponding elemental line scanning analysis (Fig. 1F) further determine the structure of Pt$_3$Co nanoflowers. Clearly, Pt and Co atoms are uniformly distributed throughout the whole nanoflower, verifying the formation of Pt$_3$Co alloys. The coexistence of Pt and Co elements in the final product is further confirmed by the EDS analysis (Fig. 1G), with the atomic Pt to Co ratio of 76.66:23.24. This value is close to 3:1.

Fig. 1H displays the XRD pattern of Pt₃Co nanoflowers (curve a), using commercial Pt black (curve b) as a reference. The two samples exhibit four representative diffraction peaks at around 40°, 47°, 68°, and 82°, corresponding to the (111), (200), (220), and (311) planes of the fcc of Pt. Impressively, the diffraction peaks for Pt₃Co nanoflowers slightly shift to higher 2θ values, compared with commercial Pt black, suggesting the reduced lattice parameter of Pt and the formation of Pt₃Co alloys [42]. Although no peaks for Co and its oxides can be found, their presence cannot be neglected because they may be present in a very small amount or even in the amorphous form [43].

The averaged crystal size can be calculated from the (220) diffraction peak based on Scherrer's equation [9], $L = (0.9\lambda)/(\beta_{1/2}\cos\theta)$ with the value of ca. 4.9 nm, where λ is the wavelength of X-ray (1.5406 Å), θ is the angle at the position of the maximum peak, and $\beta_{1/2}$ is the width of the diffraction peak at half height in radians. This value matches well with the averaged particle size obtained from HRTEM measurements.

XPS analysis was used to characterize the oxidation states of Pt₃Co nanoflowers (Fig. 2). The binding energies of 75.33 and 72.08 eV are corresponding to Pt $4f_{5/2}$ and Pt $4f_{7/2}$ (Fig. 2A), which can be divided into two pairs of doublets: metallic Pt at 75.28 and 72.03 eV, and Pt^{2+} at 76.48 and 73.13 eV [9]. The existence of Pt^{2+} is assigned to the formation of PtO [20,44]. Similarly, two pairs of doublets are deconvoluted by curve-fitting of Co $2p_{1/2}$ and Co $2p_{3/2}$ XPS regions (Fig. 2B). The stronger peaks at 797.14 and 781.13 eV are attributed to Co^0, while the weaker ones located at 802.27 and 785.68 eV correspond to Co^{2+}. The coexistence of small amount of Co^{2+} indicates the surface of Co was partially oxidized to CoO. This observation is well consistent with those in the literature [20,45,46]. By measuring their relative intensities, one can find that metallic Pt and Co are the predominant species, with the percentage of 80.1% and 60.3%, respectively, which is closely related with the catalytic activity.

Importantly, the existence of HDPC was found essential to form well-dispersed flower-like Pt₃Co nanoparticles. The absence of HDPC yields aggregated solid Pt₃Co nanoparticles, while other conditions were remained the same (Fig. 3). It indicates the key role of HDPC as a capping agent. The presence of HDPC can protect the nanoparticles form aggregation and even induce the formation of flower-like Pt₃Co nanoparticles.

Fig. 4A shows the CVs of Pt₃Co nanoflowers (curve a), solid Pt₃Co nanoparticles (curve b) and commercial Pt black (curve c) catalysts modified electrodes, in which there are two pairs of well-defined hydrogen desorption/adsorption and metal oxidation/reduction peaks. In the positive scanning, hydrogen desorption regions appear at 0−0.2 V (denoted with dotted box I), and hydroxyl species (OH_{ad}) adsorption regions emerge beyond 0.8 V (denoted with dotted box II). Besides, in the reverse scanning, the OH_{ad} reduction
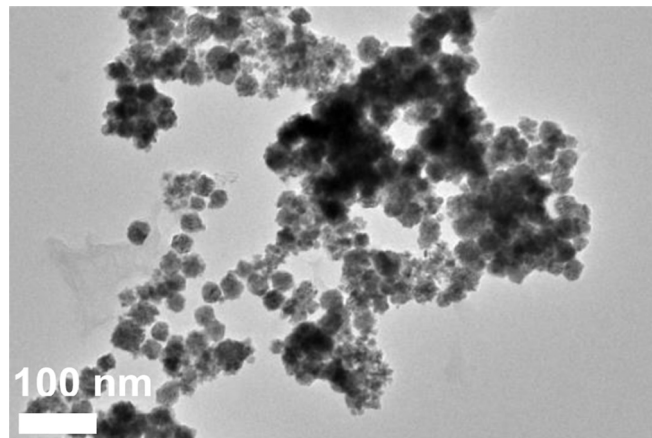

Fig. 3. TEM image of solid Pt₃Co nanoparticles prepared in the absence of HDPC.

peaks come out at 0.7−0.8 V (denoted with dotted box III), and hydrogen adsorption regions are detected below 0.2 V (denoted with dotted box IV). Notably, there is a new peak emerged at 0.72 V for Pt₃Co nanoflowers, which is ascribed to the oxidation of Co leaching from the alloyed surface [47].

Furthermore, the potentials of OH_{ad} adsorption/desorption peaks are 0.911/0.768 V for Pt₃Co nanoflowers, which positively shift compared with those of solid Pt₃Co nanoparticles (0.857/0.711 V) and Pt black (0.881/0.747 V), suggesting weak affinity of the OH_{ad} on Pt₃Co nanoflowers. Nørskov et al. firstly reported that the activity of the metal catalyst is highly depended on the energy of d-band center (ε_d) [48,49]. A lower lying d-band center tends to bind adsorbates more weakly. Therefore, the positive shifts of OH_{ad} adsorption/desorption peaks can be due to the decrease of Pt d-band center via modifying the electronic structure of Pt by Co, as confirmed by the d-band theory [50] and XPS experiments [51]. Since the adsorbed OH_{ad} species has a negative effect on MOR [20,52] and ORR [53,54], the weak affinity of OH_{ad} on surface of Pt₃Co nanoflowers facilitates the kinetics, thus improving the activities.

The ECSA is calculated from the hydrogen desorption region, with the value of 13.16 m² g⁻¹ for Pt₃Co nanoflowers. This value is higher than those of solid Pt₃Co nanoparticles (8.67 m² g⁻¹) and Pt black (10.29 m² g⁻¹) catalysts. The larger ECSA is attributed to the unique structures of Pt₃Co nanoflowers.

Fig. 4B displays the ORR polarization curves of Pt₃Co nanoflowers (curve a), solid Pt₃Co nanoparticles (curve b), and commercial Pt black (curve c) catalysts modified electrodes in O₂-saturated 0.1 M HClO₄ at a rotation rate of 1600 rpm. And the currents were normalized to the geometrical area of the modified
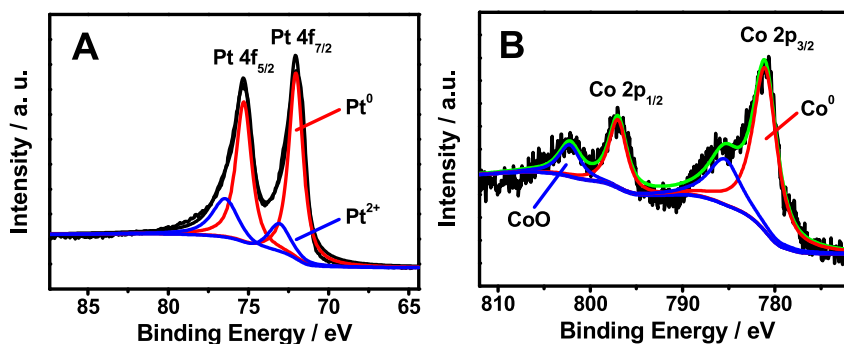

Fig. 2. High-resolution XPS spectra of (A) Pt 4f and (B) Co 2p in Pt₃Co nanoflowers.
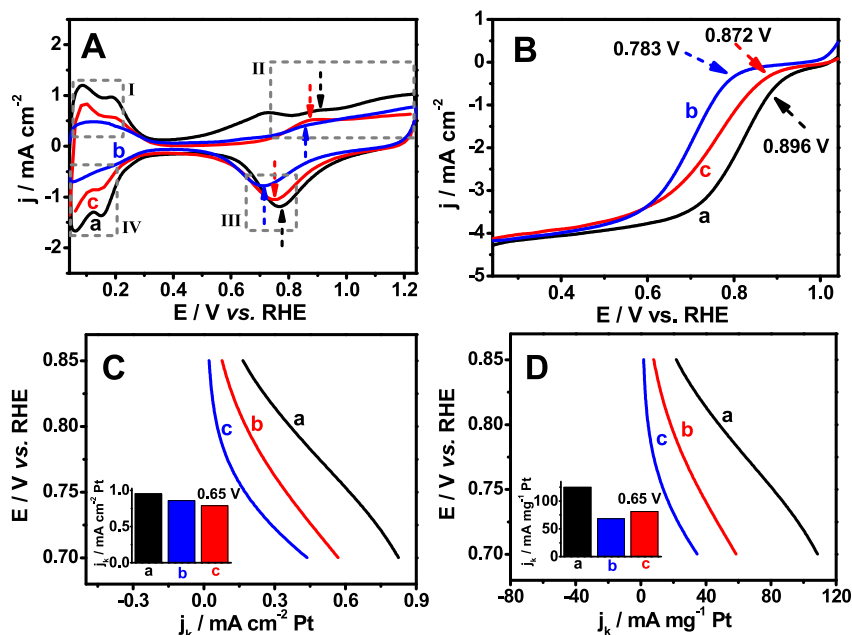
Fig. 4. (A) Cyclic voltammograms of Pt$_3$Co nanoflowers (curve a), solid Pt$_3$Co nanoparticles (curve b), and commercial Pt black (curve c) catalysts modified electrodes in 0.1 M HClO$_4$ at a scan rate of 50 mV s^{-1}. (B) The corresponding ORR polarization curves in O$_2$-saturated 0.1 M HClO$_4$ with a rotation rate of 1600 rpm and a scan rate of 5 mV s^{-1}. (C, D) The corresponding specific and mass activities given as kinetic current densities normalized against the ECSA and mass of Pt, respectively. Insets show the specific and mass activities at 0.65 V, respectively.

electrode. The onset potential is 0.896 V for Pt$_3$Co nanoflowers, which is more positive than those of solid Pt$_3$Co nanoparticles (0.783 V), and Pt black (0.872 V). Besides, the half-wave potential is 0.805 V for Pt$_3$Co nanoflowers, which is also more positive than those of solid Pt$_3$Co nanoparticles (0.703 V) and Pt black (0.741 V). These results reveal the improved catalytic activity of Pt$_3$Co nanoflowers.

In order to further estimate the intrinsic ORR activity of Pt$_3$Co nanoflowers, the kinetic currents were normalized to the real Pt surface area and Pt mass (Fig. 4C and D). Clearly, Pt$_3$Co nanoflowers display higher specific and mass activities than those of solid Pt$_3$Co nanoparticles and Pt black in the potential region of 0.70−0.85 V.

Moreover, the specific and mass activities at 0.65 V are provided (insets in Fig. 4C and D). Obviously, the specific activity is 0.951 mA cm^{-2} Pt for Pt$_3$Co nanoflowers, which is higher than those of solid Pt$_3$Co nanoparticles (0.859 mA cm^{-2} Pt) and Pt black (0.789 mA cm^{-2} Pt). Meanwhile, the mass activity is 125.08 mA mg^{-1} Pt for Pt$_3$Co nanoflowers, which is 1.70 and 1.54
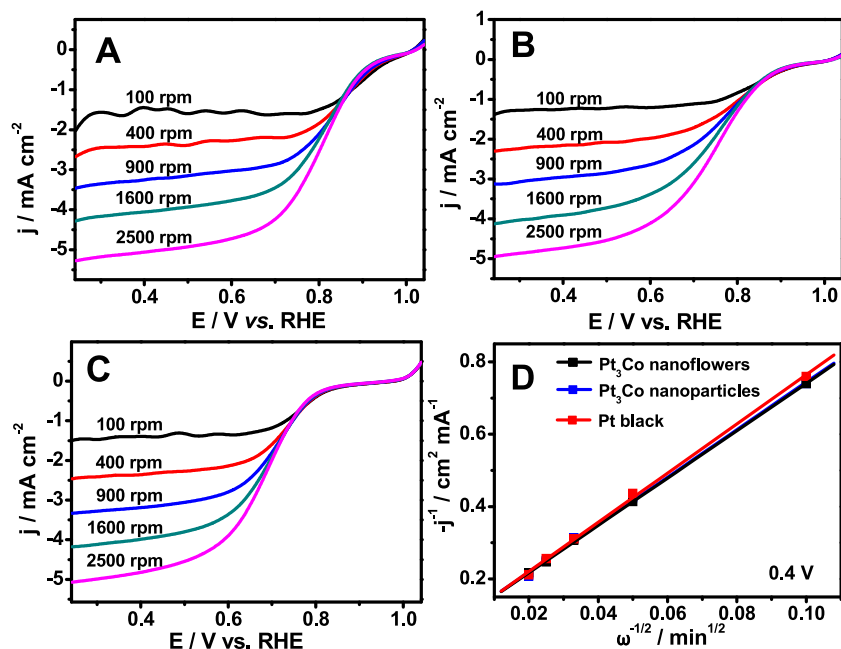

Fig. 5. Polarization curves of ORR on (A) Pt$_3$Co nanoflowers, (B) solid Pt$_3$Co nanoparticles, and (C) Pt black catalysts modified electrodes in O$_2$-saturated 0.1 M HClO$_4$ at different rotation rates with a scan rate of 5 mV s^{-1}. (D) The corresponding Koutecky−Levich plots at 0.4 V.

times larger than those of solid Pt_3Co nanoparticles (68.24 mA mg^{-1} Pt) and Pt black (81.22 mA mg^{-1} Pt), respectively. The improved ORR electrocatalysis for Pt_3Co nanoflowers is ascribed to the inhibition of Pt–OH$_{ad}$ formation via adjusting the electronic structure of Pt with Co and their unique flower-like structures. The electrocatalytic activity of Pt_3Co nanoflowers is also higher than those of core–shell-like Pt_3Co nanoparticles (0.14 mA cm^{-2} Pt) [26], Pd$_{core}$@Pt$_{shell}$ nanocatalysts (0.52 mA cm^{-2} Pt) [55], and Pt_3Ni nanoctahedras (110 mA mg^{-1} Pt) [56].

More detailed investigations of the kinetic parameters for ORR were performed on Pt_3Co nanoflowers (Fig. 5A), solid Pt_3Co nanoparticles (Fig. 5B), and Pt black (Fig. 5C) catalysts modified electrodes by altering the rotation speed from 100 to 2500 rpm at a scan rate of 5 mV s^{-1}. As illustrated in Fig. 5D, the electron transfer number is calculated to be 4.06, 4.04, and 3.91 for Pt_3Co nanoflowers, solid Pt_3Co nanoparticles, and Pt black, respectively, confirming the efficient reduction of O_2 to H_2O via the four-electron reaction pathway.

The performance of Pt_3Co nanoflowers (Fig. 6A, curve a), solid Pt_3Co nanoparticles (Fig. 6A, curve b), and Pt black (Fig. 6A, curve c) catalysts modified electrodes were further investigated for methanol oxidation reaction (MOR). Fig. 6A shows the corresponding CVs in 0.1 M HClO$_4$ + 1.0 M methanol, in which all the currents were normalized to the geometrical area of the modified electrode. The onset potential is 0.407 V for Pt_3Co nanoflowers, which negatively shift ca. 165 and 142 mV, compared with solid Pt_3Co nanoparticles (0.572 V) and Pt black (0.549 V), respectively. The down shift of the onset potential indicates the significant improvement in the kinetics of MOR [9].

Methanol oxidation is strongly characterized by the well-separated anodic peaks in the forward and reverse scans. The anodic peak current density in the forward scan (j_f) is proportional to the amount of methanol oxidized at the electrode surface [57]. Obviously, the peak current density is much higher for Pt_3Co nanoflowers, compared to solid Pt_3Co nanoparticles and Pt black. Fig. 6B shows the corresponding specific and mass activities calculated from the peak currents in the positive scans. The specific activity is 2.92 mA cm^{-2} Pt for Pt_3Co nanoflowers, which is 1.15 and

1.25 times higher than those of solid Pt_3Co nanoparticles (2.36 mA cm^{-2} Pt) and Pt black (2.34 mA cm^{-2} Pt), respectively. Moreover, the mass activity of Pt_3Co nanoflowers is 385.12 mA mg^{-1} Pt, which is much larger than those of solid Pt_3Co nanoparticles (187.47 mA mg^{-1} Pt) and Pt black (160.15 mA mg^{-1} Pt). Additionally, the catalytic activity of Pt_3Co nanoflowers is also higher than those of Pt nanoparticles/graphene (2.53 mA cm^{-2} Pt) [58], branched Pt–Ni nanocrystals (0.9 mA cm^{-2} Pt) [59], and nanoporous PtRu alloys (52.2 mA mg^{-1}) [60].

The ratio of j_f to the reverse oxidation peak current density (j_r), j_f/j_r, can be employed as an indicator for the tolerance of a catalyst to the accumulation of incompletely oxidized species such as CO. The large ratio of j_f/j_r means efficient methanol oxidation to CO_2 and elimination of poisoning species from the catalyst surface. The j_f/j_r is 1.37 for Pt_3Co nanoflowers, which is higher than those of solid Pt_3Co nanoparticles (1.32) and Pt black (1.19), implying better resistance to poisoning CO of Pt_3Co nanoflowers.

To further verify this assumption, CO stripping voltammograms were recorded on Pt_3Co nanoflowers (Fig. 6C, curve a), solid Pt_3Co nanoparticles (Fig. 6C, curve b) and Pt black (Fig. 6C, curve c) catalysts modified electrodes. Notably, the peak potential for CO oxidation is 0.776 V on the Pt_3Co nanoflowers modified electrode, which is more negative than those of solid Pt_3Co nanoparticles (0.901 V), and Pt black (0.834 V), reflecting the efficient removal of CO from Pt_3Co nanoflowers.

Herein, the enhanced CO tolerance of Pt_3Co nanoflowers can be ascribed to the ligand effects between Co and Pt, which alters the electronic structure of Pt, inducing the negative shift of Pt 4f binding energy of Pt_3Co nanoflowers and the lowering of Pt d-band center, as strongly supported by previous work [61,62]. It is known that the lowering of d-band center weakens the interactions of the adsorbates to the substrates [63–65]. Therefore, the change of electronic structure of Pt leads to the weakened CO adsorbed on Pt_3Co nanoflowers. Besides, the efficient CO removal from Pt_3Co nanoflowers is also associated with the bifunctional mechanism. The Co disrupts the continuity of Pt lattice and provides more sites for OH adsorption [20,32].
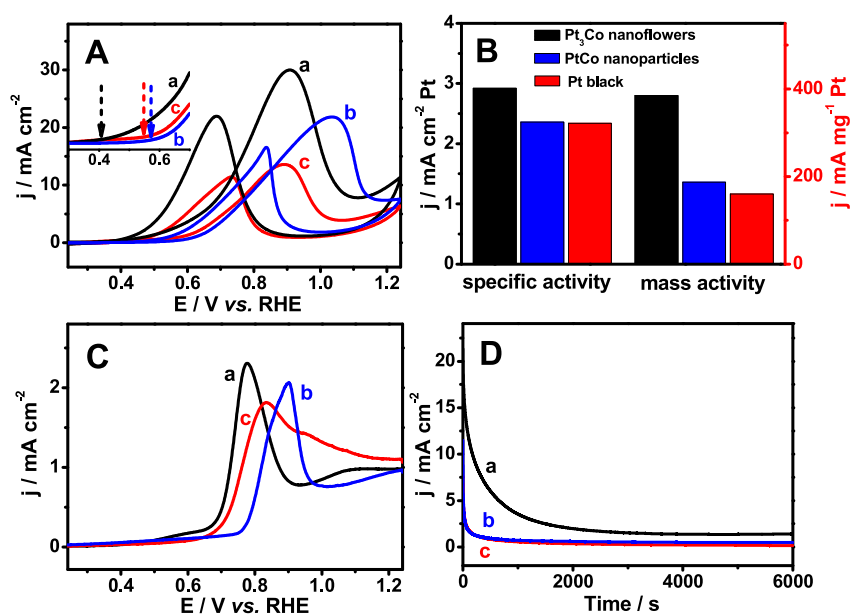

Fig. 6. (A) Cyclic voltammograms of Pt_3Co nanoflowers (curve a), solid Pt_3Co nanoparticles (curve b), and Pt black (curve c) catalysts modified electrodes in 0.1 M HClO$_4$ containing 1.0 M methanol. (B) The corresponding specific and mass activities calculated from the peak currents in the positive scans. The corresponding (C) CO-stripping voltammograms at a scan rate of 50 mV s^{-1} in 0.1 M HClO$_4$ and (D) chronoamperometric curves by applying a potential of 0.85 V in 0.1 M HClO$_4$ + 1.0 M methanol.
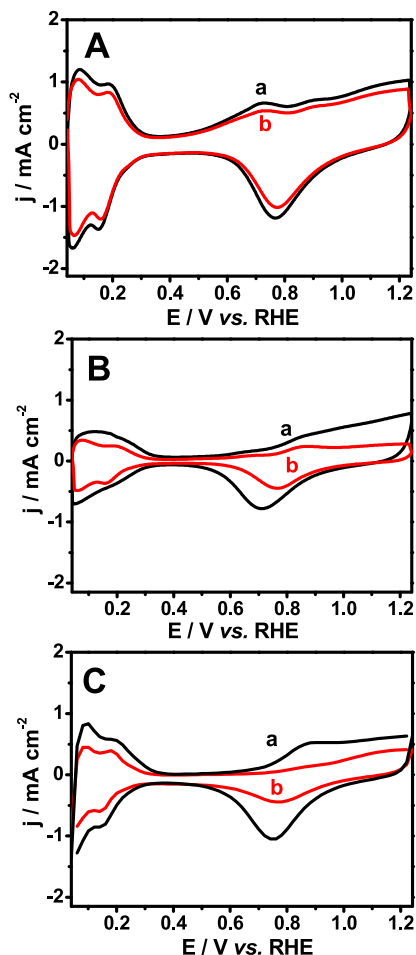
Fig. 7. Cyclic voltammograms of (A) Pt₃Co nanoflowers, (B) solid Pt₃Co nanoparticles, and (C) commercial Pt black catalysts modified electrodes before (curve a) and after (curve b) 1000 potential cycles in 0.1 M HClO₄.

oxidation current are observed for Pt_3Co nanoflowers in comparison with solid Pt_3Co nanoparticles and Pt black under the same conditions, although the current density continues to decay.

Furthermore, the accelerated durability test (ADT) was performed to examine the stability of Pt_3Co nanoflowers, using solid Pt_3Co nanoparticles and Pt black as references. After 1000 cycles, the ECSA is remained 84.38% of its initial value (Fig. 7A) for Pt_3Co nanoflowers, while the ECSA is about 53.26% and 55.94% for solid Pt_3Co nanoparticles (Fig. 7B) and Pt black (Fig. 7C) under the identical conditions, respectively. These results indicate that Pt_3Co nanoflowers have the enhanced long-term catalytic stability for MOR in acid media. The enhanced stability is attributed to the unique interconnected structures of Pt_3Co nanoflowers, which can effectively suppress the Ostwalding ripening effects [31,32]. This assumption is further supported by TEM measurements (Fig. 8), in which the flower-like structures are still remained and no obvious aggregation is found after the ADT.

4. Conclusion

A simple one-pot method was developed for synthesis of porous Pt_3Co nanoflowers via the co-reduction of $Pt(acac)_2$ and $Co(acac)_3$ in oleylamine. The alloyed Pt_3Co nanoflowers displayed the enhanced electrocatalytic performance for ORR and MOR in $HClO_4$, compared with solid Pt_3Co nanoparticles and commercial Pt black. This is ascribed to the unique interconnected porous structure, the ligand effects, and bifunctional mechanism. The as-developed method provides a general approach for preparation of bimetallic electrocatalysts in DMFCs.

Acknowledgment

To further evaluate the stability of Pt_3Co nanoflowers (Fig. 6D, curve a), solid Pt_3Co nanoparticles (Fig. 6D, curve b), and Pt black (Fig. 6D, curve c) catalysts modified electrodes, $i-t$ curves were recorded for 6000 s at a fixed potential of 0.85 V in 0.1 M $HClO_4$ + 1.0 M methanol. Apparently, the initial current density rapidly decays, due to the formation of CO-like intermediate species during MOR. However, much slower current decay and higher

References

[1] Y. Lu, Y. Jiang, H. Wu, W. Chen, J. Phys. Chem. C 117 (2013) 2926–2938.
[2] W.B. Kim, Y. Kim, Y. Noh, E.J. Lim, S. Lee, S.M. Choi, J. Mater. Chem. A 2 (2014) 6976–6986.
[3] J.-N. Zheng, S.-S. Li, X. Ma, F.-Y. Chen, A.-J. Wang, J.-R. Chen, J.-J. Feng, J. Power Sources 262 (2014) 270–278.
[4] E.A. Franceschini, M.M. Bruno, F.J. Williams, F.A. Viva, H.R. Corti, ACS Appl. Mater. Interfaces 5 (2013) 10437–10444.
[5] S. Guo, S. Dong, E. Wang, Energy Environ. Sci. 3 (2010) 1307–1310.
[6] F. Li, Y. Guo, Y. Liu, H. Qiu, X. Sun, W. Wang, Y. Liu, J. Gao, Carbon 64 (2013) 11–19.
[7] H. Zhang, M. Jin, Y. Xia, Chem. Soc. Rev. 41 (2012) 8035–8049.
[8] S.-S. Li, J.-J. Lv, Y.-Y. Hu, J.-N. Zheng, J.-R. Chen, A.-J. Wang, J.-J. Feng, J. Power Sources 247 (2014) 213–218.
[9] J.-N. Zheng, S.-S. Li, X. Ma, F.-Y. Chen, A.-J. Wang, J. Chen, J.-J. Feng, J. Mater. Chem. A 2 (2014) 8386–8395.
[10] J.-J. Lv, S.-S. Li, J.-N. Zheng, A.-J. Wang, J.-R. Chen, J.-J. Feng, Int. J. Hydrogen Energy 39 (2014) 3211–3218.
[11] X. Yu, D. Wang, Q. Peng, Y. Li, Chem. Commun. 47 (2011) 8094–8096.
[12] C. Xu, L. Wang, X. Mu, Y. Ding, Langmuir 26 (2010) 7437–7443.
[13] C.-T. Hsieh, J.-Y. Lin, J. Power Sources 188 (2009) 347–352.
[14] X.-W. Zhou, R.-H. Zhang, Z.-Y. Zhou, S.-G. Sun, J. Power Sources 196 (2011) 5844–5848.
[15] Y. Liu, D. Li, V.R. Stamenkovic, S. Soled, J.D. Henao, S. Sun, ACS Catal. 1 (2011) 1719–1723.
[16] C. Xu, Q. Li, Y. Liu, J. Wang, H. Geng, Langmuir 28 (2011) 1886–1892.
[17] T. Toda, H. Igarashi, H. Uchida, M. Watanabe, J. Electrochem. Soc. 146 (1999) 3750–3756.
[18] R. Loukrakpam, J. Luo, T. He, Y. Chen, Z. Xu, P.N. Njoki, B.N. Wanjala, B. Fang, D. Mott, J. Yin, J. Klar, B. Powell, C.-J. Zhong, J. Phys. Chem. C 115 (2011) 1682–1694.
[19] A.K. Singh, Q. Xu, ChemCatChem 5 (2013) 652–676.
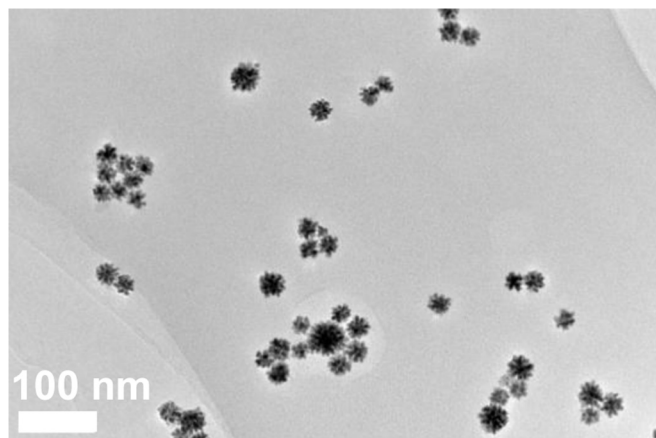[20] J. Xu, X. Liu, Y. Chen, Y. Zhou, T. Lu, Y. Tang, J. Mater. Chem. 22 (2012) 23659–23667.

Fig. 8. TEM image of Pt_3Co nanoflowers after the ADT.

[21] Q. Jiang, L. Jiang, H. Hou, J. Qi, S. Wang, G. Sun, J. Phys. Chem. C 114 (2010) 19714–19722.
[22] C. Xu, J. Hou, X. Pang, X. Li, M. Zhu, B. Tang, Int. J. Hydrogen Energy 37 (2012) 10489–10498.
[23] H. Qiu, F. Zou, ACS Appl. Mater. Interfaces 4 (2012) 1404–1410.
[24] S.-I. Choi, R. Choi, S.W. Han, J.T. Park, Chem. Eur. J. 17 (2011) 12280–12284.
[25] Q. Huang, H. Yang, Y. Tang, T. Lu, D.L. Akins, Electrochem. Commun. 8 (2006) 1220–1224.
[26] J.-H. Jang, J. Kim, Y.-H. Lee, I.Y. Kim, M.-H. Park, C.-W. Yang, S.-J. Hwang, Y.-U. Kwon, Energy Environ. Sci. 4 (2011) 4947–4953.
[27] H. Yang, J. Zhang, K. Sun, S. Zou, J. Fang, Angew. Chem. 122 (2010) 7000–7003.
[28] W. Li, Z. Chen, L. Xu, Y. Yan, J. Power Sources 195 (2010) 2534–2540.
[29] Y. Vasquez, A.K. Sra, R.E. Schaak, J. Am. Chem. Soc. 127 (2005) 12504–12505.
[30] Y. Wang, H. Yang, J. Am. Chem. Soc. 127 (2005) 5316–5317.
[31] G. Fu, K. Wu, J. Lin, Y. Tang, Y. Chen, Y. Zhou, T. Lu, J. Phys. Chem. C 117 (2013) 9826–9834.
[32] M. Gong, G. Fu, Y. Chen, Y. Tang, T. Lu, ACS Appl. Mater. Interfaces 6 (2014) 7301–7308.
[33] W. Wang, D. Wang, X. Liu, Q. Peng, Y. Li, Chem. Commun. 49 (2013) 2903–2905.
[34] F. Wang, C. Li, L.-D. Sun, C.-H. Xu, J. Wang, J.C. Yu, C.-H. Yan, Angew. Chem. Int. Ed. 51 (2012) 4872–4876.
[35] X. Huang, Y. Li, Y. Chen, E. Zhou, Y. Xu, H. Zhou, X. Duan, Y. Huang, Angew. Chem. Int. Ed. 52 (2013) 2520–2524.
[36] X. Huang, E. Zhu, Y. Chen, Y. Li, C.-Y. Chiu, Y. Xu, Z. Lin, X. Duan, Y. Huang, Adv. Mater. 25 (2013) 2974–2979.
[37] J. Xu, A.R. Wilson, A.R. Rathmell, J. Howe, M. Chi, B.J. Wiley, ACS Nano 5 (2011) 6119–6127.
[38] J. Xu, G. Fu, Y. Tang, Y. Zhou, Y. Chen, T. Lu, J. Mater. Chem. 22 (2012) 13585–13590.
[39] J. Wu, H. Yang, Nano Res. 4 (2011) 72–82.
[40] B. Luo, X. Yan, S. Xu, Q. Xue, Electrochem. Commun. 30 (2013) 71–74.
[41] H. Yang, J. Zhang, K. Sun, S. Zou, J. Fang, Angew. Chem. Int. Ed. 49 (2010) 6848–6851.
[42] S. Jiang, Y. Ma, G. Jian, H. Tao, X. Wang, Y. Fan, Y. Lu, Z. Hu, Y. Chen, Adv. Mater. 21 (2009) 4953–4956.
[43] J.R.C. Salgado, E. Antolini, E.R. Gonzalez, Appl. Catal. B 57 (2005) 283–290.
[44] C. Nethravathi, E.A. Anumol, M. Rajamathi, N. Ravishankar, Nanoscale 3 (2011) 569–571.
[45] J. Shen, B. Yan, M. Shi, H. Ma, N. Li, M. Ye, Mater. Res. Bull. 47 (2012) 1486–1493.
[46] H.T. Duong, M.A. Rigsby, W.-P. Zhou, A. Wieckowski, J. Phys. Chem. C 111 (2007) 13460–13465.
[47] C. Xu, A. Liu, H. Qiu, Y. Liu, Electrochem. Commun. 13 (2011) 766–769.
[48] J. Greeley, J.K. Nørskov, M. Mavrikakis, Annu. Rev. Phys. Chem. 53 (2002) 319–348.
[49] B. Hammer, J.K. Nørskov, Adv. Catal. 45 (2000) 71–129.
[50] J.R. Kitchin, J.K. Nørskov, M.A. Barteau, J.G. Chen, Phys. Rev. Lett. 93 (2004) 156801.
[51] M. Wakisaka, S. Mitsui, Y. Hirose, K. Kawashima, H. Uchida, M. Watanabe, J. Phys. Chem. B 110 (2006) 23489–23496.
[52] S. Wang, S.P. Jiang, T.J. White, J. Guo, X. Wang, J. Phys. Chem. C 113 (2009) 18935–18945.
[53] Z. Peng, H. Yang, J. Am. Chem. Soc. 131 (2009) 7542–7543.
[54] X. Liu, G. Fu, Y. Chen, Y. Tang, P. She, T. Lu, Chem. Eur. J. 20 (2014) 585–590.
[55] G. Zhang, Z.-G. Shao, W. Lu, H. Xiao, F. Xie, X. Qin, J. Li, F. Liu, B. Yi, J. Phys. Chem. C 117 (2013) 13413–13423.
[56] J. Zhang, H. Yang, J. Fang, S. Zou, Nano Lett. 10 (2010) 638–644.
[57] C.W. Xu, H. Wang, P.K. Shen, S.P. Jiang, Adv. Mater. 19 (2007) 4256–4259.
[58] J.-D. Qiu, G.-C. Wang, R.-P. Liang, X.-H. Xia, H.-W. Yu, J. Phys. Chem. C 115 (2011) 15639–15645.
[59] Z. Niu, D. Wang, R. Yu, Q. Peng, Y. Li, Chem. Sci. 3 (2012) 1925–1929.
[60] E.A. Anumol, A. Halder, C. Nethravathi, B. Viswanath, N. Ravishankar, J. Mater. Chem. 21 (2011) 8721–8726.
[61] S. Papadimitriou, S. Armyanov, E. Valova, A. Hubin, O. Steenhaut, E. Pavlidou, G. Kokkinidis, S. Sotiropoulos, J. Phys. Chem. C 114 (2010) 5217–5223.
[62] P. Hernández-Fernández, M. Montiel, P. Ocón, J.L.G. Fierro, H. Wang, H.D. Abruña, S. Rojas, J. Power Sources 195 (2010) 7959–7967.
[63] B. Hammer, J.K. Nørskov, Surf. Sci. 343 (1995) 211–220.
[64] M. Mavrikakis, B. Hammer, J.K. Nørskov, Phys. Rev. Lett. 81 (1998) 2819–2822.
[65] B. Hammer, Y. Morikawa, J.K. Nørskov, Phys. Rev. Lett. 76 (1996) 2141–2144.